AGU PUBLICATIONS

JGR

Journal of Geophysical Research: Space Physics

RESEARCH ARTICLE
10.1002/2014JA020910

Special Section:
Low-Frequency Waves in Space Plasmas

Key Points:
- The ion-Bernstein (IB) mode is highly unstable to proton loss cones at Mercury
- The IB mode can become highly compressional as it propagates
- Ray tracing of the IB mode predicts compression peaking the off equator

Correspondence to:
S. A. Boardsen,
Scott.A.Boardsen@nasa.gov

Citation:
Boardsen, S. A., E.-H. Kim, J. M. Raines, J. A. Slavin, D. J. Gershman, B. J. Anderson, H. Korth, T. Sundberg, D. Schriver, and P. Travnicek (2015), Interpreting ~1 Hz magnetic compressional waves in Mercury's inner magnetosphere in terms of propagating ion-Bernstein waves, *J. Geophys. Res. Space Physics*, *120*, 4213–4228, doi:10.1002/2014JA020910.

Received 2 DEC 2014
Accepted 27 APR 2015
Accepted article online 30 APR 2015
Published online 1 JUN 2015

©2015. American Geophysical Union. All Rights Reserved.

Interpreting ~1 Hz magnetic compressional waves in Mercury's inner magnetosphere in terms of propagating ion-Bernstein waves

S. A. Boardsen[1,2], E.-H. Kim[3], J. M. Raines[4], J. A. Slavin[4], D. J. Gershman[4,5], B. J. Anderson[6], H. Korth[6], T. Sundberg[7], D. Schriver[8], and P. Travnicek[9]

[1]Goddard Planetary Heliophysics Institute, University of Maryland, Baltimore County, Baltimore, Maryland, USA, [2]Heliophysics Science Division, NASA Goddard Space Flight Center, Greenbelt, Maryland, USA, [3]Princeton Center for Heliophysics and Princeton Plasma Physics Laboratory, Princeton University, Princeton, New Jersey, USA, [4]Department of Atmospheric, Oceanic and Space Sciences, University of Michigan, Ann Arbor, Michigan, USA, [5]Geospace Physics Laboratory, NASA Goddard Space Flight Center, Greenbelt, Maryland, USA, [6]Johns Hopkins University Applied Physics Laboratory, Laurel, Maryland, USA, [7]School of Physics and Astronomy, Queen Mary University of London, London, UK, [8]Department of Physics, University of California, Los Angeles, California, USA, [9]Space Science Laboratory, University of California, Berkeley, California, USA

Abstract We show that ~1 Hz magnetic compressional waves observed in Mercury's inner magnetosphere could be interpreted as ion-Bernstein waves in a moderate proton beta ~0.1 plasma. An observation of a proton distribution with a large planetary loss cone is presented, and we show that this type of distribution is highly unstable to the generation of ion-Bernstein waves with low magnetic compression. Ray tracing shows that as these waves propagate back and forth about the magnetic equator; they cycle between a state of low and high magnetic compression. The group velocity decreases during the high-compression state leading to a pileup of compressional wave energy, which could explain the observed dominance of the highly compressional waves. This bimodal nature is due to the complexity of the index of refraction surface in a warm plasma whose upper branch has high growth rate with low compression, and its lower branch has low growth/damping rate with strong compression. Two different cycles are found: one where the compression maximum occurs at the magnetic equator and one where the compression maximum straddles the magnetic equator. The later cycle could explain observations where the maximum in compression straddles the equator. Ray tracing shows that this mode is confined within ±12° magnetic latitude which can account for the bulk of the observations. We show that the Doppler shift can account for the difference between the observed and model wave frequency, if the wave vector direction is in opposition to the plasma flow direction. We note that the Wentzel-Kramers-Brillouin approximation breaks down during the pileup of compressional energy and that a study involving full wave solutions is required.

1. Introduction

Narrowband harmonic waves, whose fundamental is near the proton cyclotron frequency (f_{cp}) at the magnetic equator, are frequently observed in Mercury's inner (<2 Mercury radii (R_M), 1 R_M~2440 km) magnetosphere [*Russel*, 1989; *Boardsen et al.*, 2009a, 2009b, 2012]. The statistics of these waves are summarized in Figures 7, 8, and 9 of *Boardsen et al.* [2012]. These waves are observed between radial distances of 1.1 to 1.8 R_M, with their occurrence maximizing around 1.4 R_M, and are clustered around the magnetic equator. They occur primarily on the nightside, peaking around 21 h magnetic local time (MLT). There is also a secondary peak in the postmidnight sector. These waves are observed primarily between magnetic latitudes of ±40°. The wave power is observed to maximize around the magnetic equator.

Of the wave events near the magnetic equator, 75% of the events are compressionally dominant, with magnetic compressibility $(\delta b_{||}/\delta b)^2 > 0.5$, while the other 25% are transverse dominant [*Boardsen et al.*, 2012]. The latter are believed to be either ion cyclotron waves and/or field-line resonances [*Russell*, 1989; *Othmer et al.*, 1999; *Kim and Lee*, 2003; *Klimushkin et al.*, 2006; *Kim et al.*, 2008, 2011, 2013, 2015]. The transition from compressional to transverse dominance occurs roughly at magnetic latitudes of ±20° [*Boardsen et al.*, 2012]. The goal of this paper is to explore a possible explanation for the strongly compressional wave events in terms of a local plasma instability.

Large planetary ion loss cone distributions believed to be present in Mercury's inner magnetosphere can be highly unstable to the generation of plasma waves. These distributions are believed to be present because Mercury's internal magnetic field is weak relative to Earth's field, and therefore, warm plasma sheet plasma can penetrate deep into Mercury's inner magnetosphere. The planetary loss cone varies from ~20° to ~67° as the radial position varies from 2.0 to 1.1 R_M, so as the plasma sheet ions move deeper into the inner magnetosphere, the ion distribution functions develop large loss cones.

If Mercury had a cold plasma population, then the strong magnetic compressibility could be explained in terms of the extraordinary mode from cold plasma theory excited by the ion-Bernstein instability [e.g., *Perraut et al.*, 1982; *Boardsen et al.*, 1992; *Gary et al.*, 2011] and the waves at Mercury would be similar to the strong compressional waves observed in the Earth's inner equatorial magnetosphere [e.g., *Perraut et al.*, 1982]. But Mercury is believed to have no cold plasma component, due to the lack of an ionosphere as a cold plasma source, and because the corotational electric field, if it exists, which is necessary for confinement, is very weak due to the low planetary rotation period of 59 days. So the cold plasma extraordinary mode cannot be used to explain the compressional waves at Mercury.

Based on instability studies by *Denton et al.* [2010] and *Gary et al.* [2010] using warm plasma with no cold component in the Earth's plasma sheet boundary layer, *Boardsen et al.* [2012] proposed that these compressional waves at Mercury could be mainly composed of short wavelength ~100 km "electromagnetic" ion-Bernstein mode waves in a high beta proton plasma. The electromagnetic ion-Bernstein mode has been definitively identified in plasma sheet boundary layer at Earth [*Engebretson et al.*, 2010; *Denton et al.*, 2010; *Gary et al.*, 2010] and tentatively identified in the solar wind [*Joyce et al.*, 2012].

The term electromagnetic is used loosely, since the longitudinal (along $k_{||}$) electric field component of the wave dominates its transverse component [e.g., *Denton et al.*, 2010], suggesting "electrostatic," but the magnetic perturbations associated with this mode become readily detectable when proton beta becomes large enough, with $E/Bc < 1$. The perpendicular component of the wave vector ($k_\perp$) of the ion-Bernstein mode is much greater than the parallel component ($k_{||}$) with wave normal angles near 90°. The peak growth occurs at frequencies just below but very close to the proton cyclotron frequency and its harmonics [*Denton et al.*, 2010; *Gary et al.*, 2010].

As proton beta (β_P) increases, the ion-Bernstein wave transition from the electrostatic ion-Bernstein mode for $\beta_P \sim 5 \times 10^{-4}$ to a magnetic transverse dominant electromagnetic mode for $\beta_P \sim 0.4$ (observed in the Earth's plasma sheet boundary layer) and to a magnetic compressional dominant electromagnetic mode for $\beta_P \sim 2$ [*Denton et al.*, 2010]. Except in magnetic cavities (plasma sheet proper) at Mercury [*Korth et al.*, 2011; *Korth et al.*, 2014; *Gershman et al.*, 2014, 2015], such high beta are not observed. In this paper we use warm plasma ray tracing and show that in a smaller beta plasma of ~0.1, waves that are initially transverse dominant can become compressionally dominant in a cyclic manner as they propagate in a trapped magnetic (dipole) geometry.

In this preliminary study, we model the growth and propagation of this mode in a dipole field with a constant plasma density and proton loss cone source throughout the ray tracing volume. We launch waves at peak growth rates at the fundamental at 1.35 R_M, varying the initial equatorial proton beta in the range of 0.05 to 0.54 for the different traces. This paper is organized as follows. In the observation section we present an example of a compressional dominant wave event and corresponding proton moments (Figure 1) and show a highly time averaged proton loss cone distribution (Figure 2) for the event shown in Figure 1. In the instability and ray tracing analysis section, using parameters based on the observations, we show that the proton loss cone distribution (Figure 3a) is highly unstable to the generation of low compressional waves (Figure 3b) and that as the waves propagate, they become highly compressional (Figures 4–7) in a cyclic manner. We show that the compressional wave energy piles up due to a decrease in group velocity around peak compression (Figure 9). In the discussion section we attempt to reconcile the location of the observed frequency peaks with that predicted by linear theory using the Doppler shift between the spacecraft and the bulk plasma flow frame of reference (Figure 10). We suggest that the observations of the compression peaking just off the magnetic equator (Figure 11) as opposed to right at the equator are consistent with the findings of our ray tracing.

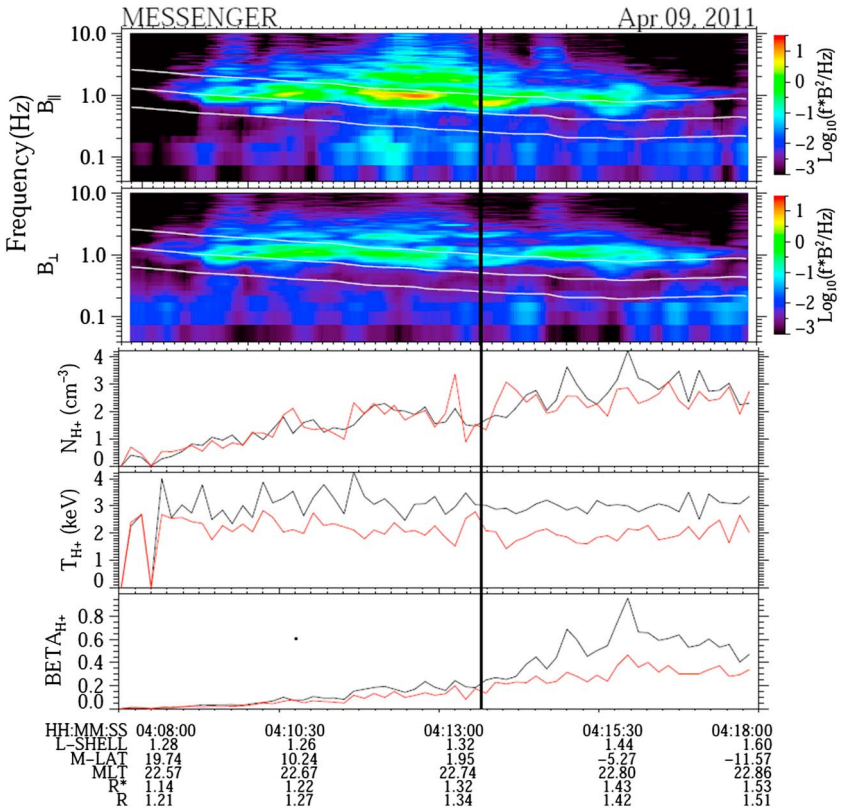

Figure 1. Dynamic spectra of the magnetic (first panel) compressional and (second panel) transverse components for frequency values between 0.04 and 10 Hz, along with the (third panel) proton density, (fourth panel) proton temperature, and (fifth panel) proton beta are plotted. The compressional (transverse) component is power spectral density along (perpendicular) to the background magnetic field. On the spectrograms the white lines are at the proton cyclotron frequency, the He^{++} cyclotron frequency, and the He^{+} cyclotron frequency. The model magnetic equator is given by the black vertical line. R^* is the distance from the offset planetary dipole. In the fourth to fifth panels the red line is a Maxwellian fit and the black line is a moment of the FIPS proton data. The peak wave power seen in the compressional component occurs just below the proton cyclotron frequency and is associated with a proton beta in the 0.1 to 0.2 range.

2. Observations

An example wave event is shown in Figure 1. The top two panels are frequency-time spectrograms of the magnetometer data, which are sampled at 20 s^{-1} [*Anderson et al.*, 2007]. The first panel shows the power spectral density of the compressional magnetic component, while the second panel is of the power spectral density of the transverse magnetic components. Around 04:12 UT a strong enhancement in wave power is observed, which occurs chiefly in the compressional component, just below the proton cyclotron frequency (~0.8 f_{cp}). Note a weaker enhancement in the compressibility in the southern hemisphere around 04:14 UT. The solid vertical black bar indicates the model magnetic equator crossing, which is offset by +0.19 R_M along the planet's spin axis from the planetary equator [*Anderson et al.*, 2008, 2010, 2011]. The magnetic latitude and magnetic *L* shell is computed relative to this offset. The waves are observed between magnetic latitudes of approximately −12° to 14°.

The proton measurements associated with these waves are shown in the third to the fifth panels. These measurements are derived from analysis of the Fast Imaging Plasma Spectrometer (FIPS) proton scan data. FIPS measures protons and heavier ions in the 50 to 13,000 eV/q range over a 1.40π sr field of view of which 1.15π sr are not obscured by the spacecraft body itself or its appendages [*Raines et al.*, 2011]. Due to telemetry constraints, the scan data consists of the proton counts, which are averaged on board over the entire field of view per energy channel, the angular information is lost. The averaged counts per energy channel have been converted to differential flux from which moments (black line) and Maxwellian fits (red line) have been made [*Raines et al.*, 2011, 2013]. Estimates of the proton density, temperature, and

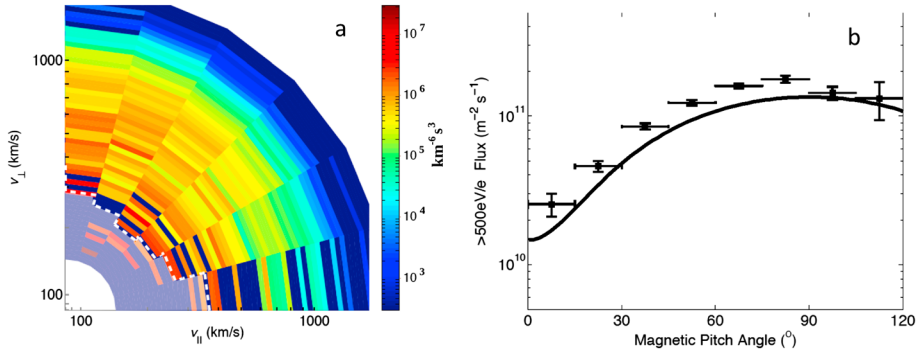

Figure 2. (a) FIPS proton pitch angle distribution for pitch angles between 0 and 90°; note that the pitch angles up to 120° were measured. The distribution was computed by averaging over the entire time interval shown in Figure 1. (b) Integral of differential flux versus pitch angle for proton energies >500 eV. The solid curve is the integral of differential flux versus the pitch angle for proton energies >500 eV from the model proton distribution for run 5 in Table 1 of this study.

beta (β_P) are plotted in the third, fourth, and fifth panels, respectively. The fluctuations in the moments are mainly due to low counting statistics. Proton beta in the range of 0.1 to 0.2 is observed for this event around maximum wave power.

Can we see large loss cones in the proton distribution function? Besides proton scan data, which retain no angular information, data consisting of individual proton counts with both energy and angular information are available, from which pitch angle distributions can be computed [e.g., *Gershman et al.*, 2014]. Due to telemetry constraints, the individual proton counts are heavily decimated on board the spacecraft before being telemetered; therefore, to get reasonable statistics, the entire 10 min time interval had to be used in computing the average proton pitch angle distribution. The average proton energy versus pitch angle distribution for the entire time interval of Figure 1 is plotted in Figure 2a; note that for this interval, FIPS had pitch angle measurements ranging from 0 to 120°; the pitch angle bin size is 15°. The integral of the proton differential flux over the energy range of 0.5 to 13 keV versus pitch angle is shown in Figure 2b. The solid line in Figure 2b is the integral of the model phase space density used for run 5 in Table 1 converted to proton differential flux and then integrated over the energy range of 0.5 to 13 keV. The loss cone is clearly present. We point out that the estimated planetary loss cone varies from 63° at the start of this interval down to 32° at the end of this interval. The average loss cone weighted by moment-derived density (shown in Figure 1) is 40°. The field line-traced equatorial loss cone at the peak of the compressional wave emissions at 04:12 UT is ~45°. Figures 2a and 2b show that there are particles within the minimum planetary loss cone at pitch angles less than 32°; the likely scattering mechanism is through interaction with these waves.

Knowledge of the electron temperature is also needed for the instability and ray tracing analysis. MESSENGER has no instrument that measures electrons in the critical energy range of 0 to 2 keV. The Mariner-10 measurements of the mean electron energy in the central plasma sheet is 1 keV, which decreases to 100 to 200 eV at the edges of the plasma sheet, with typical electron densities in the 0.1 to 1 cm^{-3} range [*Ogilvie et al.*, 1977]. The ion instrument had failed by the time of the Mariner-10 Mercury flybys, so the ratio of the electron to ion temperature was not determined. For the MESSENGER mission, the proton temperature and density in Mercury's plasma sheet tail are observed in the range from 0.4 to 2.6 keV and from 1 to 10 cm^{-3}, respectively [*Gershman et al.*, 2014], density values greater than those of the Mariner-10 flybys. *Ogilvie et al.* [1977] noted that the properties of the electrons in Mercury's plasma sheet were similar to that of the Earth's plasma sheet. In the Earth's plasma sheet, the observed ratio of the proton to electron temperature is in the range of 0.1 to 0.25 [*Baumjohann et al.*, 1989; *Wang et al.*, 2012]. For this study we use electron to proton temperature ratio of 0.125 for the majority of the runs.

The effects of heavy ions are not included in this preliminary study. Here we note typical values for the heavy ions. *Gershman et al.* [2014] found that the energy of the planetary ions is ~1.5 times the proton energy in the plasma sheet and that near the dusk side magnetopause, the Na^+ density is about 0.1 times the proton density [*Gershman et al.*, 2014]. We note that the average Na^+ density in the 18:00–24:00 MLT sector below an attitude of 2000 km, where the wave events peak, is between 0.03 and 0.001 cm^{-3}

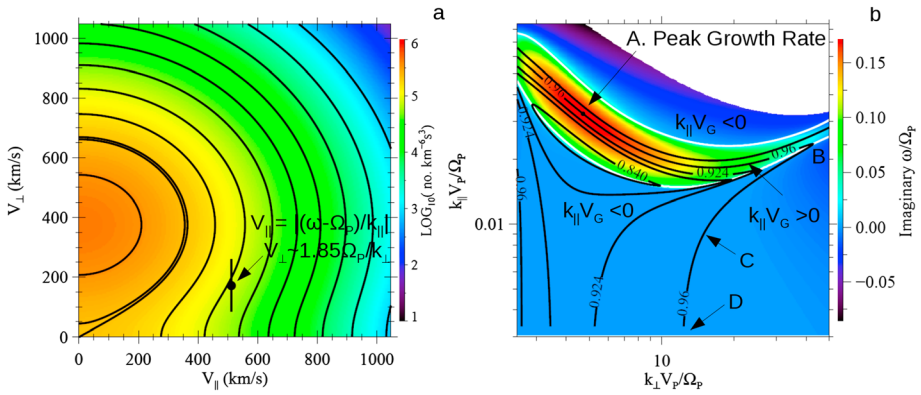

Figure 3. (a) The proton velocity phase space distribution function used in the instability and warm plasma ray tracing code, formed by a difference of two bi-Maxwellians to approximate a loss cone distribution, using parameters for run 3 in Table 1. The region where the protons strongly interact with the waves at peak wave growth is indicated by the dot. (b) The imaginary part of the dispersion surface computed using the distribution of Figure 3a is shown in normalized coordinates; V_P is the proton thermal speed, and Ω_P is the angular proton cyclotron frequency. The red color is the strong growth, the dark blue color is the strong damping. The index of refraction surface (black curve) that contains maximum growth rate, whose frequency is 0.96 f_{cp}, at point A is laid on top. The surface is characterized by an upper branch (A-B) and a lower branch (B-D). Strong wave growth and mild compression are associated with the upper branch, while weak growth/damping and strong compression are associated with the lower branch. The index of refraction curves for frequency values of 0.84, 0.924, and 1 (upper curve) f_{cp} are also plotted. The white curves are boundaries where the product of $V_{G||}$ $k_{||}$ change signs.

(Figure 3b of *Raines et al.* [2013]). The ratio of He^{++} to H^+ in the plasma sheet is observed to be 2.5% [*Gershman et al.*, 2014]. Having characterized the waves and their plasma environment, we focus on instability analysis and warm plasma ray tracing.

3. Instability Analysis

We use Waves in Homogeneous Anisotropic Magnetized Plasma (WHAMP) [*Rönnmark*, 1982, 1983a] to solve the dispersion relation. WHAMP has been used in many peer-reviewed studies [e.g., *Rönnmark*, 1983b; *André*, 1985; *André*, 1986; *André et al.*, 1986; *Boardsen et al.*, 1992; *Menietti et al.*, 2002; *Janhunen et al.*, 2003; *Denton et al.*, 2010; *Wu et al.*, 2013]. WHAMP is a nonrelativistic dispersion relation solver where the plasma distribution functions are specified by the sums and differences of bi-Maxwellian distribution functions for each plasma species (both ions and electrons). The formula for the distribution function used by WHAMP is shown below for species *j*, where in this study *j* is either protons or electrons.

$$f_j(V_\perp, V_{||}) = n_j\left(\pi^{1/2}V_j\right)^{-3}\exp\left(-\left(\frac{V_{||}^2}{V_j^2}\right)\right)\left[\frac{D}{A}\exp\left(\frac{-V_\perp^2}{AV_j^2}\right)+\frac{1-D}{A-B}\left(\exp\left(\frac{-V_\perp^2}{AV_j^2}\right)-\exp\left(\frac{-V_\perp^2}{BV_j^2}\right)\right)\right] \quad (1)$$

where $V_\perp$, $V_{||}$ are the perpendicular and parallel components of the particle velocity, and n_j is the density of species *j*. To maintain quasineutrality, the electron (n_e) and proton (n_p) densities are equal. $V_j \equiv (2\ T_j/m_j)^{1/2}$ is the parallel thermal speed of species *j*, T_j is the parallel temperature, and m_j is the mass. *A* (*B*) is the perpendicular to parallel temperature ratio of the added (subtracted) components, and *D* is the depth of the loss cone; for $D = 0$, the loss cone is deep, while for $D = 1$, there is no loss cone. For this preliminary study the same values for the *A*, *B*, and *D* parameters are used for both protons and electrons.

Input parameters used in WHAMP are given in columns 4 to 9 in Table 1, which are the electron density (n_e); the parallel proton (T_p) and electron (T_e) temperature; and the parameters *A*, *B*, and *D*. Columns 2 and 3 give the proton (β_P) and electron (β_e) betas used for each ray tracing run. Looking at Figure 1, the fitted densities around peak compression is ~2 cm^{-3}, and the fitted proton temperatures is ~2 keV. For ray tracing, we use densities in the range of 0.5 to 2 cm^{-3} and a proton temperature of 1 keV (lower than that of the event of Figure 1 but a typical value when looking at a number of events).

As noted that the planetary loss cones vary from 63° at the start of this interval down to 32°, we adjusted the parameters *A*, *B*, and *D* such that the slope of the iso-phase space density contour that intersects the origin is

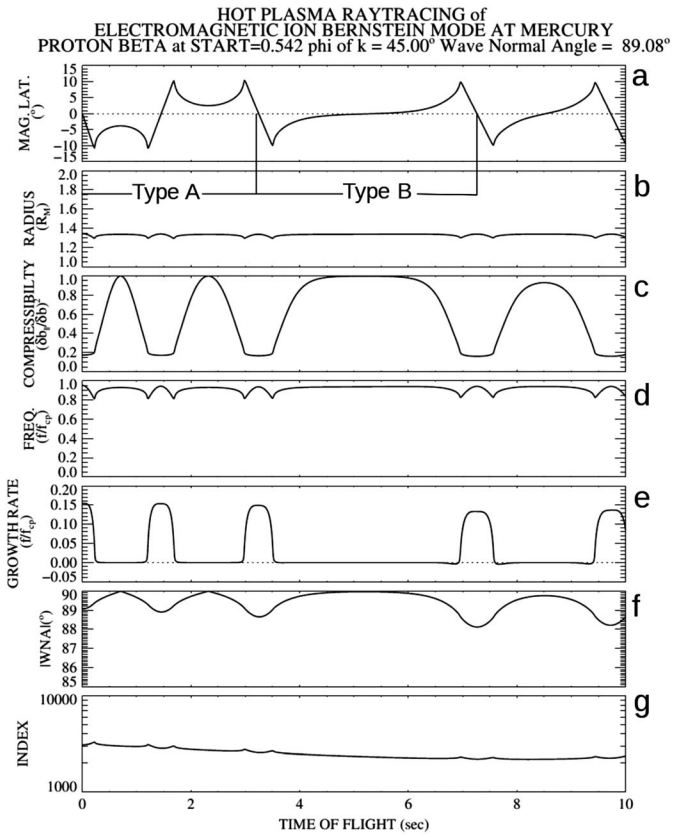

Figure 4. Ray tracing of the fundamental of the ion-Bernstein mode for a plasma with a proton beta of 0.542 at the launch point is shown, using parameters from run 6 in Table 1, for an initial azimuth angle of 45°. Panels represent the following: (a) the magnetic latitude, (b) the radial position, (c) the magnetic compressibility, (d) the frequency normalized by f_{cp}, (e) the growth/damping rate, (f) the absolute value of the wave normal angle, and (g) the index of refraction. As the wave propagates, it toggles between the upper and lower branches of the index of refraction surface. The lower branch gives high compression, while the upper branch gives high growth rate.

about 30° at low velocities, the low end of the range of planetary loss cone angles over the time interval of Figure 1. For a comparison of the model with the observed phase space density distribution, the integral of the model differential flux is compared with the observed integral of the differential flux for a model density of $2\,cm^{-3}$ in Figure 2b. The comparison is reasonable. An example of the proton plasma distribution function used in our analysis is shown in Figure 3a, computed using parameters from run 3 of Table 1.

We compute the dispersion surface for the fundamental using the parameters from run 3 in Table 1.

The growth/damping rate is plotted in Figure 3b as a function of $k_{||}$ and $k_{\perp}$, normalized by the thermal proton gyroradius $\rho_P = V_P/\Omega_P$. The index of refraction (IOR) surface (black curve) containing maximum growth rate is shown on top of the growth/damping rate of the dispersion surface. The IOR surface has an upper branch (A-B), which is a region of strong growth rate with moderate to minimum compression.

We note that around peak growth rate, our solutions are similar to those found by *Denton et al.* [2010] and *Gary et al.* [2010] in the Earth's plasma sheet boundary layer. *Denton et al.* [2010] and *Gary et al.* [2010] use a proton shell distribution as the source of the instability. The peak growth rate (Figure 3b) occurs at $k_{\perp}V_P/\Omega_P \sim 5$, so the wavelength of the fundamental at peak growth rate is near the thermal proton gyroradius consistent with the findings of *Denton et al.* [2010] and *Gary et al.* [2010].

IOR curves are shown for different values of f/f_{cp} to give the reader a feeling for how this surface changes as the wave propagates. The white curves on the plot are boundaries indicating where the parallel component of the group velocity changes sign, which is critical in understanding how the wave propagates as explained later.

At large normalized wave number of ~30, the IOR upper branch (A-B) connects to the lower branch (B-D). The lower branch (B-D) is a region of weak growth or damping that becomes strongly compressional as $|k_{||}|$ approaches 0. It is the strong compressional nature of this lower branch that makes this wave mode a good candidate for explaining the compressibility of the observed waves, not the upper branch as originally proposed in *Boardsen et al.* [2012]. As mentioned, a proton beta of ~2 would be required for the upper branch to be compressional [*Denton et al.*, 2010], such that beta is only observed in the plasma sheet tail at Mercury [*Korth et al.*, 2014; *Gershman et al.*, 2015], where these waves are not observed.

The region where maximum energy exchange between the waves and the protons is located on the proton distribution function is important because there are limitations as to how well a loss cone can be approximated by the difference of two bi-Maxwellians. For example, at $V_{||} = 0$, the distribution function

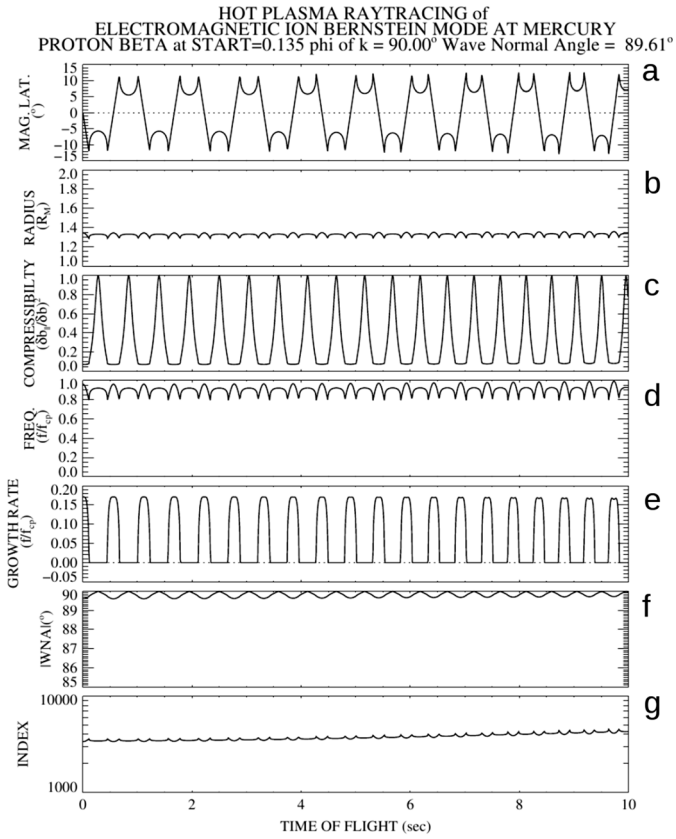

Figure 5. Ray tracing of the fundamental of the electromagnetic ion-Bernstein mode for a plasma with a proton beta of 0.135 at the launch point is shown, using parameters from run 3 in Table 1, for an initial azimuth angle of 90° (azimuthal direction). Note that the peak in magnetic compression straddles the magnetic equator.

looks more like a ring distribution than a loss cone distribution, so we want to verify that maximum energy exchange is occurring near the edge of the loss cone. The protons strongly interact with these waves through the ion cyclotron resonance condition $\omega - k_{||}v_{||} = n\Omega_P$ where ω is the angular wave frequency, Ω_P is the angular proton cyclotron frequency, $v_{||}$ is the parallel particle velocity, and n is the harmonic number. While electrons, because $k_\perp \gg k_{||}$, interact with these waves through Landau damping, $\omega = k_{||}v_{||}$. For the protons, the region in the distribution function that contributes to the bulk of the growth is given by the resonance condition plus the maximum of $J_n(k_\perp v_\perp/\Omega_P)^2$ [*Schmidt*, 1979, p. 264] where J_n is the Bessel function of the first kind and $v_\perp$ is the perpendicular proton speed. For the fundamental ($n = 1$), this maximum occurs at $k_\perp v_\perp/\Omega_P = 1.85$. The region of maximum interaction for the wave solution at maximum growth rate is indicated by the bar with a dot centered on it in Figure 3a, which lies near the loss cone edge. The size of the bar indicates the full width at half maximum of J_n^2. This point lies near the edge of a loss cone, albeit at a pitch angle of 20° instead of 30°.

Using the values given in Table 1, we have computed similar index of refraction curves at the start of each run. We find that the shape of the index of refraction surface using different electron temperatures ranging from 0.001 T_P to 1 T_P is qualitatively similar to that shown in Figure 3b. However, we find that the electron temperature influences the peak growth rate through Landau damping. Runs 2–4 of Table 1 show that the peak growth rate decreases as the electron temperature increases: for a 1 eV electron temperature, the normalized peak growth rate is 0.190, while for a 1 keV electron temperature, the normalized peak growth rate drops to 0.112. We note that *Gary et al.* [2010] found a similar dependence of the growth rate as the electron temperature is varied. The electron temperature also influences the value of the normalized frequency at peak wave growth, the normalized frequency at peak growth decreases as the electron temperature increases.

The group velocity (V_G) also decreases as beta increases. Table 1 gives the angle of the group velocity with respect to the background field (ψ_G), and it ranges in value from 0.01° to 1° at the launch point of each run. Note that the x and y axes of Figure 3b are not plotted at the same scale, if plotted on the same linear scale, the index of refraction surface would appear as a horizontal line and the group velocity is normal to this surface (i.e., field-aligned). Having discussed the index of refraction surface containing peak growth rate, next we discuss the ray tracing of this mode.

4. Ray Tracing Analysis

Because the dispersion relation cannot be approximated by a cold plasma disperation relation, we need to perform warm plasma ray tracing; we use the code RATRACE [*Rönnmark and André*, 1991]. The code

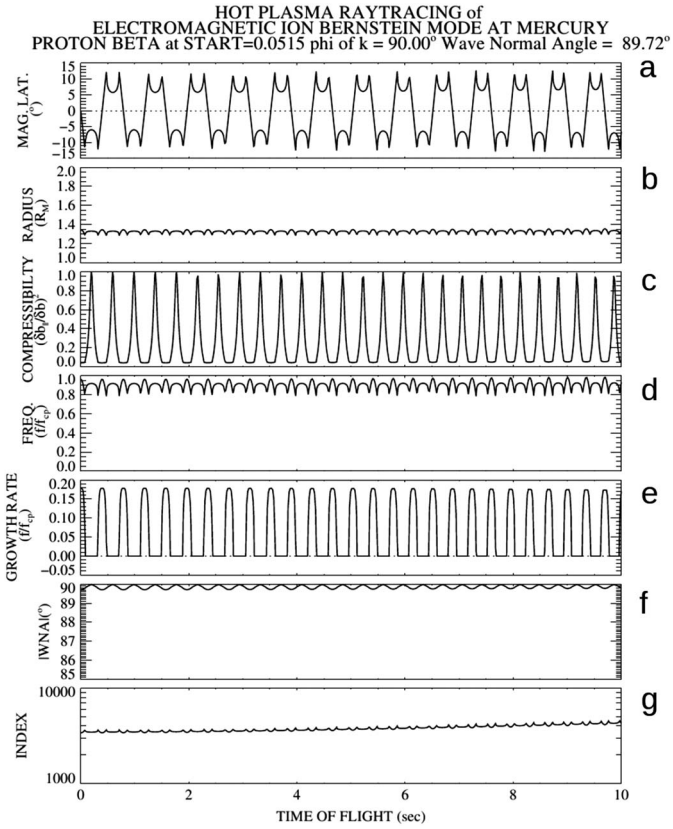

Figure 6. Ray tracing of the fundamental of the electromagnetic ion-Bernstein mode for a plasma with a proton beta of 0.051 at the launch point is shown, using parameters from run 1 in Table 1, for an initial azimuth angle of 90°.

RATRACE solves a system of nonlinear equations (equation (1) in *Rönnmark and André* [1991]), which includes weak dissipation [*Suchy*, 1981; *Rönnmark*, 1984], to trace a ray in space given by an initial wave vector at an initial position. The wave propagation is determined by the following system of first order differential equations.

$$\dot{r} = \Re\left[-\frac{\partial D}{\partial k}\Big/\frac{\partial D}{\partial \omega}\right] \quad (2)$$

$$\dot{k} = \Re\left[\frac{\partial D}{\partial r}\Big/\frac{\partial D}{\partial \omega}\right] \quad (3)$$

where the dispersion relation $D(r, \omega, k) = 0$ along all points of the ray trace, where r is the position vector, k is the wave vector, and ω is the angular wave frequency. The dispersion relationship is solved using WHAMP at each point on the raypath. In the limit of no dissipation, equation (2) reduces to the group velocity in a nondissipative medium, and equation (3) reduces to a differential form of Snell's law.

RATRACE requires that the parameters given in columns 4 to 9 of Table 1 plus the vector background magnetic field be specified throughout the ray tracing volume along with their spatial derivatives. For this preliminary study the parameters in columns 4 to 9 of Table 1 are fixed throughout the ray tracing volume and a magnetic field model represented by a magnetic dipole field with a moment of 190 nT/R_M^3 is used. For each run we launch rays at their optimal growth rate and wave normal angle (given in columns 10–12 in Table 1), starting at the magnetic equator at a radial distance of 1.35 R_M from the dipole center, where the occurrence of these waves is observed to peak. At the start of each run, the azimuthal angle of the wave vector must also be given to fully specify the wave vector direction; it can range from 0° to 360°: for azimuthal angles of 0°, 90°, and 180°, the wave vector is directed radially outward, in the azimuthal direction, and radially inward, respectively. Before discussing the wave propagation in a qualitative manner, it is simpler to show the quantitative ray tracing solutions first, computed using RATRACE.

Time series plots of the ray tracing solution are given in Figures 4–7 for different initial equatorial β_P and azimuthal angles. The raypaths shown in Figure 4 are launched for an initial β_P of 0.542 with azimuthal angles of 45°. While those in Figures 5 and 6 are, both launched in the azimuthal direction with an initial β_P of 0.135 or 0.051, respectively, and Figure 7 is launched at the third harmonic with an initial β_P of 0.051. Looking at Figures 4–7, one can see that the rays propagate in a cyclic manner between the hemispheres. Each cycle is composed of (1) segments with high growth rate (Figures 4e, 5e, 6e, and 7e) and low/moderate compression (Figures 4c, 5c, 6c, and 7c) that propagate from one hemisphere to the other and (2) segments of low growth/damping rate and high compression that propagate from one hemisphere to the other or (3) segments with low growth/damping rate and high compression that refract away from the equator in the middle of the segment.

Each time the ray refracts back toward the magnetic equator, the ray switches from a segment with high growth rate and low/moderate compression to a segment with low growth/damping rate and high compression. The segments combine to form two types of propagation cycles as indicated in Figure 4, labeled Type A and Type B. When the initial β_P is lowered to values of 0.271 to 0.051 as shown in

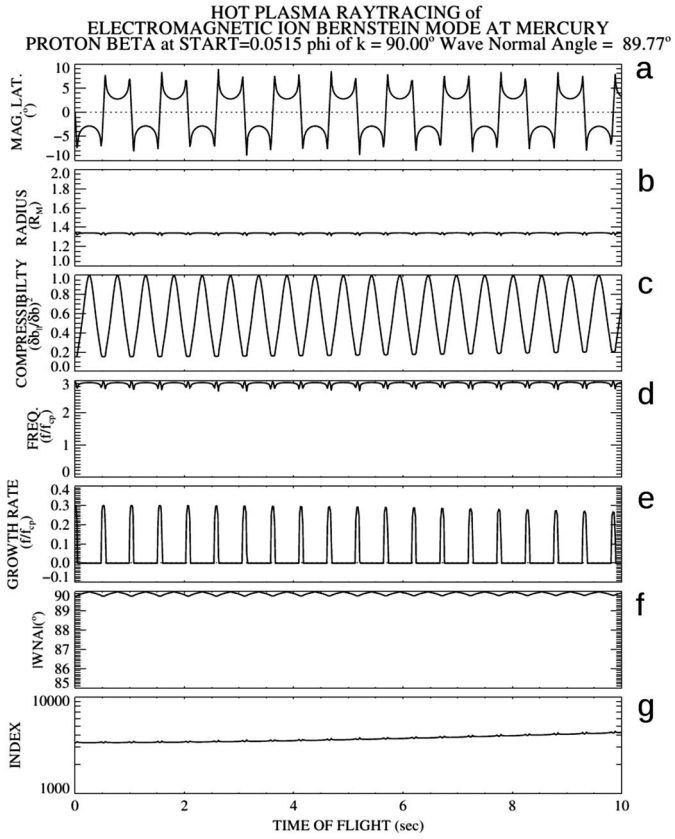

Figure 7. Ray tracing of the third harmonic of the electromagnetic ion-Bernstein mode is shown for a plasma with a proton beta of 0.051 at the launch point, using parameters from run 7 in Table 1, for an initial azimuth angle of 90°.

Figures 5–7, only one cyclic solution (Type A) has been observed where the highly compressional solution does not cross the magnetic equator. We have not found Type B for this range of β_P. We now give a qualitative explanation for the cyclic propagation.

Figure 8 shows segments of the IOR surface at different magnetic latitudes along the raypath (given in Figure 5) that contains the raypath solution (black dot in each panel) at that location. The perpendicular and parallel components of the IOR surface are plotted as $k_\perp V_P/\Omega_{P0}$ and $k_{||}V_P/\Omega_{P0}$, where Ω_{P0} is the angular cyclotron frequency at the equatorial launch point. The segments are colored black if the group velocity is away ($k_{||}V_{G||} > 0$) from the magnetic equator, red if the group velocity is toward ($k_{||}V_{G||} < 0$) the magnetic equator. In Figure 5 the ray is launched in the azimuthal direction at peak growth rate and it will travel away from the equator nearly along the magnetic field line (Figure 8a). As the ray travels up the field line, f/f_{cp} decreases because B increases (Figure 8b). Because the gradient of the medium at the launch point is in radial direction, the component perpendicular to the gradient will be approximately conserved from Snell's law (strictly conserved if the medium is planar stratified; e.g., Figure 4.42 of *Gurnett and Bhattacharjee* [2005]), indicated by the vertical line in Figure 8. A point is reached (Figure 8c) where the ray solution hits the edge of the IOR surface (in the approximately conserved direction); at this point, the ray will move onto the part of the IOR surface (red segment) where $k_{||}V_{G||} < 0$ and the ray will start to propagate back toward the equator. As the ray continues to propagate back toward the equator, f/f_{cp} increases (Figure 8d). When the ray hits the edge of the IOR surface at $k_{||} = 0$ (Figure 8e), $V_{G||}$ changes sign as $k_{||}$ changes sign and the ray starts to propagate away from the equator, and you have cycle Type A. If the ray reaches the equator before reaching $k_{||} = 0$, f/f_{cp} starts to increase upon crossing the equator, and you have cycle Type B.

5. Pileup of Compressional Energy

It is not clear from Figures 4 to 7 why the wave observations should be compressionally dominant, because as the waves propagate, they cycle between being compressional and transverse dominant. However, as the waves propagate through maximum compression, there is a strong decrease in group velocity, and if we assume that the Poynting flux is conserved, there will be a sharp ramp up in the wave amplitude while going through this minimum in group velocity. Figure 9 shows the first 0.6 s of the trace from run 3 in Table 1; one can see a sharp spike in the wave electric (Figure 9c) and magnetic (Figure 9b) fields as the wave propagates through this group velocity minimum at peak compression. This pileup suggests why compressional dominance is observed. However, the strong ramp up in wave amplitudes occurs in less than 1 wavelength implying that the Wentzel-Kramers-Brillouin (WKB) approximation is probably violated around that point.

Table 1. Plasma Parameters at the Launch Point Used in the Ray Tracing[a,b]

Run	β_P	β_e	n_e	T_p	T_e	A	B	D	X_R	X_I	ψ	V_G	ψ_G	G
1	0.051	0.006	0.19	1	0.125	1	0.9	0.2	0.964	0.179	89.72	0.030	0.17	2.2
2	0.135	0.000	0.50	1	0.001	1	0.9	0.2	0.974	0.190	89.54	0.020	0.41	4.9
3	0.135	0.017	0.50	1	0.125	1	0.9	0.2	0.962	0.171	89.60	0.021	0.35	4.8
4	0.135	0.135	0.50	1	1.000	1	0.9	0.2	0.938	0.112	89.49	0.013	0.48	3.1
5	0.271	0.034	1.00	1	0.125	1	0.9	0.2	0.959	0.164	89.40	0.014	0.61	4.6
6	0.542	0.068	2.00	1	0.125	1	0.9	0.2	0.953	0.154	89.07	0.009	1.01	3.9
7	0.051	0.006	0.19	1	0.125	1	0.9	0.2	2.968	0.300	89.77	0.044	0.01	2.0

[a]Parameters: n_e is the electron number density in cm^{-3}; β_p and β_e are the proton and electron betas, respectively; T_p and T_e are the parallel proton and electron temperatures in keV, respectively; A, B, and D are the input parameters for WHAMP that specify the shape of the velocity space distribution function; X_R and X_I are the frequency and the maximum growth rate normalized by the proton cyclotron frequency; ψ is the wave normal angle in degrees; V_G is the group velocity normalized by the speed of light; and ψ_G is the angle in degrees of the group velocity with respect to the background field direction.
[b]The path integrated *e*-folding for a launch azimuthal angle of 90° integrated over 10 s is given in the last column *G*. The launch point in each ray tracing run is in the magnetic equatorial plane, at 1.35 R_M from the dipole center where the dipole model background field is 78 nT. Run 7 was for the third harmonic, the rest are for the fundamental. Ray tracing results for runs 6, 3, 1, and 7 are given in Figures 4–7, respectively.

6. Violation of the WKB Approximation Around Peak Compression

Geometrical ray tracing requires that the Wentzel-Kramers-Brillouin (WKB) approximation holds for all points along the raypath [*Whitman*, 1999; *Gurnett and Bhattacharjee*, 2005]; this is satisfied if the wavelength is much shorter than the spatial-scale lengths in the media. We estimate the spatial-scale length L at the equator as $r/3$ (the dipole field strength divided by its gradient), where the radial distance $r = 1.35\ R_M$ and the maximum wavelength λ estimated from the minimum of the IOR (bottom graph of Figures 4–7) of 2000 at a frequency of 1.2 Hz, so one gets $L = 1100$ km and $\lambda = 120$ km. Therefore, in terms of the wavelength being smaller than the spatial scales, we feel reasonably confident that the primary criteria for the WKB approximation hold. However, as noted, around $k_{||} = 0$, there is a sharp increase in wave amplitude occurring over a distance much shorter than the wavelength; therefore, one can interpret this as a violation of the WBK approximation. Additional studies, beyond the scope of this preliminary study, are needed to explore the wave propagation through $k_{||} = 0$, and possible mode conversion, and the effects of cutoffs and resonances introduced by including heavy ions. In the next section we compare the results of our preliminary ray tracing with observations and discuss limitations of our study and possible future investigations.

7. Discussion

We focus on several topics that influence the interpretation that these waves are composed of chiefly the ion-Bernstein mode: (1) Can we explain the difference between the observed wave frequencies and the frequencies at peak wave growth from linear theory using the Doppler shift? (2) How well does this mode explain the compression? (3) The comparison of magnetic latitude extent between observations and the ray tracing.

1. One major difficulty in reconciling these waves with an ion-Bernstein mode is the difference in frequency between that of the observed waves and the frequency at maximum compression predicted from ray tracing. For example, in Table 2, the observed f/f_{cp} of the fundamental is in the range of 0.63 to 0.76, while for the ray tracing example, in run 3, f/f_{cp} at maximum compression is 0.92. From the values in Table 2, the required shift to resolve the difference between observation and ray tracing in units f_{cp} is in the range of 0.16 to 0.29. Can we explain the difference by the Doppler shift between waves generated in the plasma flow frame and observed in the spacecraft frame of reference? The Doppler shift between the plasma flow frame and the spacecraft frame is given by

$$\omega_{sc} = \omega + \vec{k} \cdot \vec{V}_F \tag{4}$$

where V_F is the flow velocity. Since $\omega/k = V_P$, where V_P is the phase velocity, equation (4) can be rewritten as

$$\omega_{sc} = \omega\left(1 + \left(\hat{k} \cdot \hat{V}_F\right)\frac{V_F}{V_P}\right) \tag{5}$$

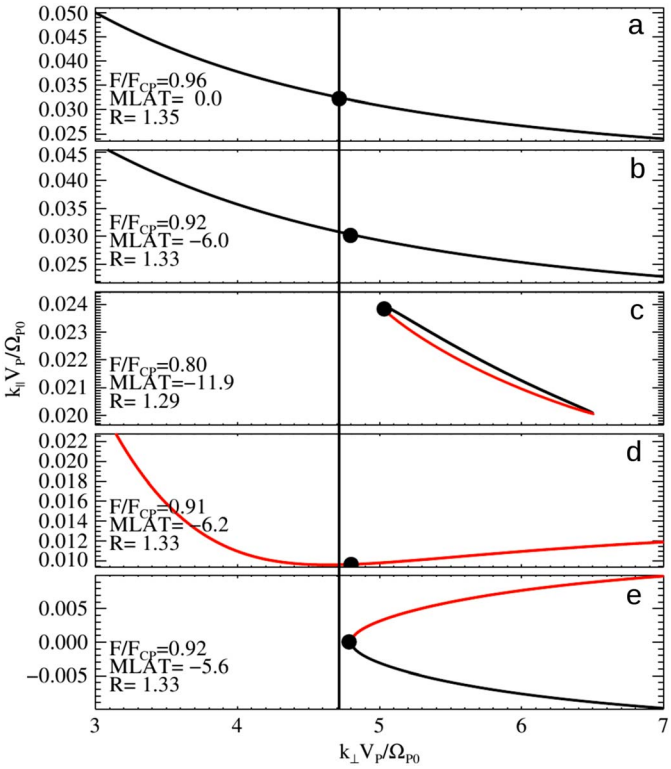

Figure 8. Segments of the index of refraction curves are plotted at various points for the ray trace solution shown in Figure 5a, in units of Ω_{P0}/V_P, where Ω_{P0} is the angular cyclotron frequency at the launch point. The black dots are the ray tracing solutions: (a) at the start, (b) between the start and first reflection, (c) at the point where the ray is reflected back toward the equator, (d) between the first two reflections, and (e) at the point where the ray is reflected away from the equator. The index of refraction surface is black where the group velocity is directed away from the equator, and red where the group velocity is directed toward the equator. The perpendicular component of the wave vector at the launch point, indicated by the black vertical line, is approximately conserved as the ray propagates.

For the first and third harmonics of runs 1 and 7, the phase velocity is about 91 km/s. Approximating ω as $n\Omega_\theta$ equation (5) gives the following for the normalized Doppler shift:

$$\Delta f/f_{cp} = n\ \ k{\cdot}V_F/(kV_F)V_F/V_P \quad (6)$$

Since the V_P is approximately constant for the lower harmonics, the Doppler shift should be roughly proportional to harmonic number. Figure 10 shows an example where this holds for the first three harmonics. To shift the model frequency down to the observed values, $k \cdot V_F$ must be less than zero. For $k \cdot V_F/(kV_F)) = -1$, using a phase speed of 91 km/s, the flow velocity must be in the 14 to 26 km/s range for observed shifts of 0.16 to 0.29.

The flow speed has been estimated from statistical studies of the estimated cross-tail potential of Mercury's magnetosphere [*Slavin et al.*, 2009; *Dibraccio et al.*, 2013]. From Figure 12 of *Dibraccio et al.* [2013], the cross-tail potential is estimated to be 29 ± 28 kV. This potential is based on measurements of the magnetic field normal to the magnetopause surface and assumes that the magnetosheath flow speed is 200 km/s. For a tail width of 3 R_M the cross-tail potential gives a cross-tail electric field of 4.0 ± 3.8 mV/M. Using a background field strength of 88 nT (Figure 1) with the cross-tail electric field estimates, the $E \times B$ drift velocity is estimated to be in the range of 45 ± 43 km/s. Superimposed upon this drift, 1 keV protons would have a gradient-curvature drift of ~5 km/s. We therefore conclude that plasma flow speed can produce the required Doppler shifts.

Because the plasma is flowing, there is a question of whether the waves can grow to sufficient amplitude as they are carried along by the plasma. In the 10 s used in our ray tracing examples, a plasma drifting at 45 km/s will travel 0.18 R_M in the sunward direction. If the perpendicular component of the group velocity at maximum growth rate is 38 km/s and the average flow speed 45 km/s, then if the wave vector is antiparallel to the flow speed at maximum growth, the wave packet position will be roughly quasi-stationary in the *x-y* plane. During the compressional phase of the wave propagation, the perpendicular component of the group velocity drops to ~0 km/s and the wave packet is carried with the flow. So as the wave cycles back and forth between its high growth rate phase and its high compressional phase, it will cycle between being nearly quasi-stationary and being carried by the flow.

This hypothesis, that the wave vector is antiparallel to the flow direction, suggests that the optimal location for growth would be in the dawn and dusk sectors when the sunward flow is tangent to a surface of constant *L* shell; at this location the waves will remain in resonance for a longer period as they are swept downstream. Waves generated at midnight will be swept across *L* shell and therefore not stay in resonance for a long time. This is somewhat consistent with the observed peak in wave events at 21 h MLT with a secondary peak at 3 h MLT in Figure 7g of *Boardsen et al.* [2012]. However, for this interpretation to hold, one must come up with a

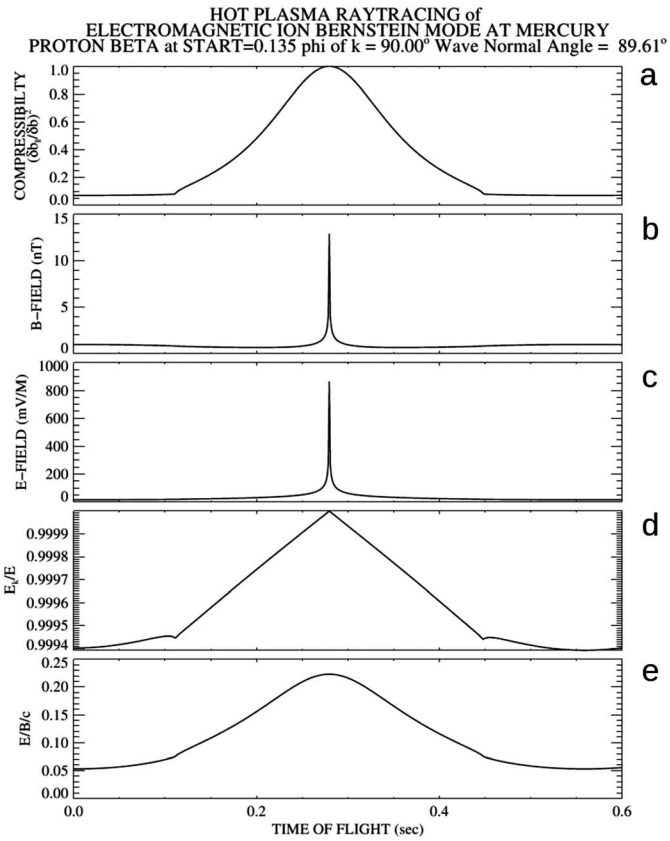

Figure 9. The first 0.6 s from run 3 in Table 1 and Figure 5 is shown. Panels represent the following: (a) the magnetic compressibility, (b) the magnetic wave amplitude, (c) the electric field wave amplitude, (d) the ratio of the electric field along k to the total electric field, and (e) the electric to magnetic wavefield ratios. The spike in amplitude is due to the minimum in group velocity as $k_{||}$ goes through zero, allowing a pileup of compressional wave energy.

mechanism that would at least partially deflect the sunward flow around Mercury. The current ray tracing models are not set up to handle flow perpendicular to the magnetic field in a 3-D geometry. Such models are needed to correctly compute the path integrated gain.

This hypothesis predicts a preferred orientation of the perpendicular component of the wave vector that would result in the discussed Doppler shift. This preferred orientation would also explain why a Doppler splitting is not observed. If the wave vectors are uniformly distributed in azimuth, one predicts a Doppler splitting [*Boardsen et al.*, 1990]. We have found only a handful of spectrograms for which the frequency structure might be attributed to a Doppler splitting; in general, there is little evidence of a Doppler splitting in our spectrograms. Our hypothesis is that nature picks out the solution with maximum wave gain, the solution where the sum of the group and flow velocities is minimized in Mercury's frame of reference.

How well does this mode explain the compression? For the Type B cycle the compression maximizes at the equator, while for the Type A cycle the compression maximizes off the equator in of range of −4 to −7° and 4 to 7° magnetic latitude, based on the ray tracing examples in Figures 4–7. As noted, we found the Type B cycle only for the highest equatorial proton beta 0.542 ray traced, the lower equatorial beta ray tracings only showed the Type A cycle. Such off equatorial enhancements have been observed in the data, for example, in Figure 11 (taken from Figure 11 of *Boardsen et al.* [2012]), where enhancements in the compressional components are observed to straddle the magnetic equator. *Boardsen et al.* [2012] suggested that off equatorial plasma sheet boundary layer crossings are the cause of the enhancements, but they also noted that the plasma sheet boundary layer crossings are not apparent in the data, so the Type A (i.e., Figure 5) cycle might be a better explanation.

Table 2. Third Column: Frequency (f) at Peak Compression, Fourth Column: Frequency Normalized by f_{cp}, Fifth to Seventh Columns: Location, and Eighth Column: Harmonic Number[a]

No.	YYYY DDD (dd/mm) hh:mm:ss.sss	f (Hz)	f/f_{cp}	R*	MLAT	MLT	H
1	2011 088 (29/3) 02:36:38.302	0.88	0.63	1.33	−1.12	1.82	1
2	2011 105 (15/4) 17:10:02.167	0.84	0.66	1.34	1.66	21.3	1
3	2011 105 (15/4) 17:10:02.167	1.75	1.37	1.34	1.66	21.3	2
4	2011 105 (15/4) 17:11:13.292	0.76	0.64	1.39	−1.82	21.3	1
5	2011 105 (15/4) 17:11:13.292	1.53	1.30	1.39	−1.82	21.3	2
6	2011 099 (9/4) 04:12:39.956	0.99	0.76	1.31	3.00	22.7	1
7	2011 099 (9/4) 04:13:50.789	0.77	0.74	1.36	−0.60	22.8	1

[a]Item 1 is from Figures 2 and 3 of *Boardsen et al.* [2012], items 2–5 are from Figure 9, and items 6 and 7 are from Figure 1.

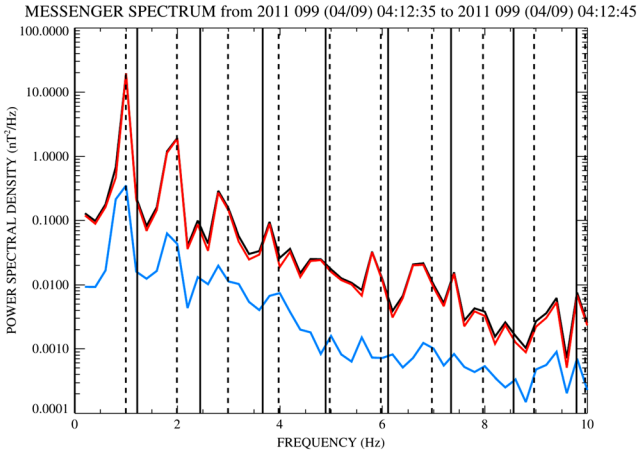

Figure 10. Spectrum from the event shown in Figure 1. The red curve is the compressional component, while the blue curve is the transverse component. The solid vertical lines are at the proton cyclotron frequency and its harmonics. The dashed vertical lines are at harmonics of the spectral peak of the fundamental.

For the Type A or B cycle the group velocity on the upper branch tends to be higher than that of the lower branch, so from conservation of Poynting flux, the overall wave amplitude of the ray will be smaller at the equator, which could explain the drop in total power spectral density (see Figure 9b) that is observed between the compressional enhancements of Figure 11. We have frequently observed these off equatorial enhancements, similar to that of Figure 11, but have not quantified their occurrence. More qualitative analysis is required in future studies. In statistical studies, we suspect that the deviation of the true magnetic equator in latitude from the average magnetic equator (using the scaling of ~8 between Mercury's and Earth's magnetosphere [*Slavin et al.*, 2008], 1.35 R_M is equivalent to 11 Earth radii at Earth) which is used in Figure 9 of *Boardsen et al.* [2012] smears out the scatter so a decrease in compression if present at the equator is not observed in the statistics.

The last topic we address is the latitudinal extent of the ray tracing compared to that of the observations. The latitudinal extent of the ray tracing is about ±12° magnetic latitude (MLAT) (Figures 4–7), compared to that of Figure 7h of *Boardsen et al.* [2012], where the bulk of the compressional observations are within ±20°, with a transverse dominant tail that extends to 60° magnetic latitude. In this preliminary study we only launched rays at maximum growth rate at the equator; launching rays at maximum growth rate off the equator should broaden the latitudinal range of the rays. Also, the latitudinal extent of wave propagation at different radial equatorial launch points was not explored. The deviation of the true magnetic equator from the model equator as the solar wind and IMF driving conditions change will also broaden the wave observations in magnetic latitude compared to that of the model. We suspect that the ion-Bernstein mode can explain the latitudinal extent for the bulk of the compressional observations.

Due to the strong linearity of these waves, one cannot accurately estimate the azimuthal direction of the waves using only magnetic field data; electric field data are needed. Unfortunately, MESSENGER does not have an electric field instrument. Figure 9d gives the ratio of the electric field along the wave vector divided by the electric field magnitude. One can see that this component dominates, so analysis of the electric fields associated with waves can be used to determine if a preference in the azimuthal direction exists. Figure 9e gives the *E*/*B* ratio; MESSENGER has observed compressional waves with peak to peak amplitude up to ~10 nT (Figure 3 of *Boardsen et al.* [2012]), which from the *E*/*B* ratio curve, one would predict a peak to peak wave electric field on the order 300 mV/M from linear theory.

Ray tracing cannot predict the nonlinear evolution and saturation of these waves. Therefore, nonlinear modeling of the growth and saturation of these waves is needed. The wave electric field is largely along the wave vector; therefore, the displacement current is not critical and hybrid simulation could be used to study these waves. Hybrid simulation [*Winske and Omidi*, 1993; *Hu and Denton*, 2009; *Hu et al.*, 2010] has been performed for ion cyclotron waves (ICW) in a 2-D dipole geometry [*Omidi et al.*, 2011, 2013]; presumably, a similar analysis could be performed replacing the anisotropic proton distribution in the ICW simulation with a loss cone distribution in order to simulate the ion-Bernstein mode.

8. Conclusion

We show that magnetic compressional waves, with $(\delta b_{||}/\delta b)^2 > 0.5$, at frequency value of ~1 Hz observed within Mercury's inner magnetosphere could be interpreted as ion-Bernstein waves in a moderate proton beta ~0.1 plasma. An observation of a highly compressional wave event was presented along with plasma

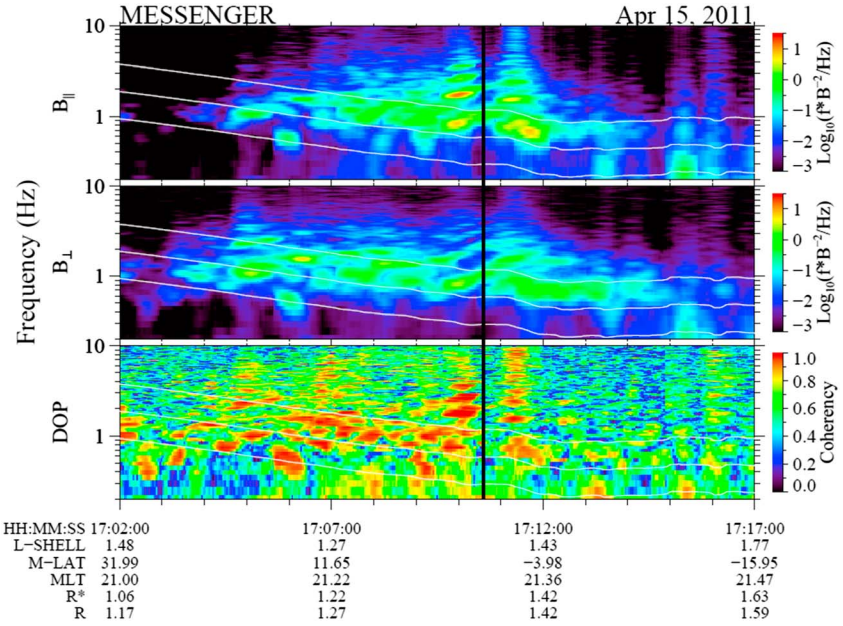

Figure 11. Taken from Figure 11 of *Boardsen et al.* [2012]. The peak emissions are observed to straddle the magnetic field. The top plot shows the compressional component, the middle plot shows the transverse component, and the bottom plot shows the degree of polarization. Ray tracing predicts (see Figure 5) a maximum in the compression that straddles the equator.

moments of the protons, whose proton beta is in the range of 0.1 to 0.2 around peak wave amplitude. The waves exhibit a harmonic frequency structure whose fundamental is close to 0.8 f_{cp}, near the magnetic equator. The waves were observed between −12° and 14° magnetic latitude. An observation of a highly time averaged proton distribution with a large planetary loss cone is presented for this event, and we show that this type of distribution is highly unstable to the generation of ion-Bernstein waves with low magnetic compression.

We studied the propagation of this unstable mode with warm plasma ray tracing. In this preliminary study the ion plasma is described by proton loss cone distribution approximated by the difference of two bi-Maxwellians, which was used as both the wave source and its carrier. No other ion species were included. The plasma density and the parameters specifying the shape of the proton loss cone were constant throughout the ray tracing volume. The magnetic field was approximated by a dipole. The only model parameter that we varied between runs was the plasma density, which we changed to vary the proton beta in the range of 0.05 to 0.54 at the ray tracing launch point.

We launched rays at peak growth at the equator at 1.35 R_M. We found that as these waves propagate back and forth about the magnetic equator they cycle between a state of low and high magnetic compression. The group velocity decreases during the high compression state leading to a pileup of compressional wave energy, which could explain the observed dominance of the highly compressional waves around the magnetic equator.

This bimodal nature is due to the complexity of the index of refraction surface in a warm plasma whose upper branch has high growth rate with low compression, and its lower branch has low growth/damping rate with strong compression. Two different cycles are found: one where the compression maximum occurs at the magnetic equator (found only for beta of 0.54) and one where the compression maximum straddles the magnetic equator (found for all beta explored). The later cycle could explain observations where the maximum in compression straddles the equator, peaking off the equator. Ray tracing shows that this mode is confined within ±12° magnetic latitude, which can account for the bulk of the observations.

We show that the Doppler shift can account for the difference between the observed and modeled wave frequency, if the wave vector direction is in opposition to the plasma flow direction. We note that the WKB

approximation breaks down during the pileup of compressional energy and that a study involving full wave solutions is required.

Acknowledgments

We thank K. Rönnmark at Umeå University in Sweden for providing us with the warm plasma instability code WHAMP and the warm plasma ray tracing code RATRACE. The data used in this study are publicly available at the Planetary Data System (http://pds.nasa.gov/). This research was supported by NASA Planetary Data Analysis Program grant NNX10AU26G and Geoscience grant NNX08AJ78G. The work at the Princeton University was supported by NASA grants NNH09AK63I and NNH11AQ46I, and DOE contract DE-AC02-09CH11466. The MESSENGER project is supported by the NASA Discovery Program under contracts NAS5-97271 to the Johns Hopkins University Applied Physics Laboratory. This work was also supported by the NASA Heliophysics Supporting Research Program under grant NNX15AJ68G.

Yuming Wang thanks Fritz M. Neubauer and another reviewer for their assistance in evaluating this paper.

References

Anderson, B. J., M. H. Acuña, D. A. Lohr, J. Scheifele, A. Raval, H. Korth, and J. A. Slavin (2007), The Magnetometer instrument on MESSENGER, *Space Sci. Rev.*, *131*, 417–450, doi:10.1007/s11214-007-9246-7.

Anderson, B. J., M. H. Acuña, H. Korth, M. E. Purucker, C. L. Johnson, J. A. Slavin, S. C. Solomon, and R. L. McNutt Jr. (2008), The structure of Mercury's magnetic field from MESSENGER's first flyby, *Science*, *321*, 82–85, doi:10.1126/science.1159081.

Anderson, B. J., et al. (2010), The magnetic field of Mercury, *Space Sci. Rev.*, *152*, 307–339, doi:10.1007/s11214-009-9544-3.

Anderson, B. J., C. L. Johnson, H. Korth, M. E. Purucker, R. M. Winslow, J. A. Slavin, S. C. Solomon, R. L. McNutt Jr., J. M. Raines, and T. H. Zurbuchen (2011), The global magnetic field of Mercury from MESSENGER orbital observations, *Science*, *333*, 1859–1862, doi:10.1126/science.1211001.

André, M. (1985), Dispersion surfaces, *J. Plasma Phys.*, *33*, 1–19, doi:10.1017/S0022377800002270.

André, M. (1986), Electrostatic ion waves generated by ion loss-cone distributions in the magnetosphere, *Ann. Geophys.*, *4*, 241–246.

André, M., M. Temerin, and D. Gorney (1986), Resonant generation of ion waves on auroral field lines by positive slopes in ion velocity space, *J. Geophys. Res.*, *91*(A3), 3145–3151, doi:10.1029/JA091iA03p03145.

Baumjohann, W., G. Paschmann, and C. A. Cattell (1989), Average plasma properties in the central plasma sheet, *J. Geophys. Res.*, *94*, 6597, doi:10.1029/JA094iA06p06597.

Boardsen, S. A., D. A. Gurnett, and W. K. Peterson (1990), Double-peaked electrostatic ion cyclotron harmonic waves, *J. Geophys. Res.*, *95*(A7), 10,591–10,598, doi:10.1029/JA095iA07p10591.

Boardsen, S. A., D. L. Gallagher, D. A. Gurnett, W. K. Peterson, and J. L. Green (1992), Funnel-shaped, low-frequency equatorial waves, *J. Geophys. Res.*, *97*(A10), 14,967–14,976, doi:10.1029/92JA00827.

Boardsen, S. A., B. J. Anderson, M. H. Acuña, J. A. Slavin, H. Korth, and S. C. Solomon (2009a), Narrow-band ultra-low-frequency wave observations by MESSENGER during its January 2008 flyby through Mercury's magnetosphere, *Geophys. Res. Lett.*, *36*, L01104, doi:10.1029/2008GL036034.

Boardsen, S. A., J. A. Slavin, B. J. Anderson, H. Korth, and S. C. Solomon (2009b), Comparison of ultra-low-frequency waves at Mercury under northward and southward IMF, *Geophys. Res. Lett.*, *36*, L18106, doi:10.1029/2009GL039525.

Boardsen, S. A., J. A. Slavin, B. J. Anderson, H. Korth, D. Schriver, and S. C. Solomon (2012), Survey of coherent 1 Hz waves in Mercury's inner magnetosphere from MESSENGER observations, *J. Geophys. Res.*, *117*, A00M05, doi:10.1029/2012JA017822.

Denton, R. E., M. J. Engebretson, A. Keiling, A. P. Walsh, S. P. Gary, P. M. E. Décréau, C. A. Cattell, and H. Rème (2010), Multiple harmonic ULF waves in the plasma sheet boundary layer: Instability analysis, *J. Geophys. Res.*, *115*, A12224, doi:10.1029/2010JA015928.

DiBraccio, G. A., J. A. Slavin, S. A. Boardsen, B. J. Anderson, H. Korth, T. H. Zurbuchen, J. M. Raines, D. N. Baker, R. L. McNutt Jr., and S. C. Solomon (2013), MESSENGER observations of magnetopause structure and dynamics at Mercury, *J. Geophys. Res. Space Physics*, *118*, 997–1008, doi:10.1002/jgra.50123.

Engebretson, M. J., C. R. G. Kahlstorf, J. L. Posch, A. Keiling, A. P. Walsh, R. E. Denton, M. C. Broughton, C. J. Owen, K.-H. Fornaçon, and H. Rème (2010), Multiple harmonic ULF waves in the plasma sheet boundary layer observed by Cluster, *J. Geophys. Res.*, *115*, A12225, doi:10.1029/2010JA015929.

Gary, S. P., K. Liu, D. Winske, and R. E. Denton (2010), Ion Bernstein instability in the terrestrial magnetosphere: Linear dispersion theory, *J. Geophys. Res.*, *115*, A12209, doi:10.1029/2010JA015965.

Gary, S. P., K. Liu, and D. Winske (2011), Bernstein instability driven by suprathermal protons in the ring current, *J. Geophys. Res.*, *116*, A08215, doi:10.1029/2011JA016543.

Gershman, D. J., J. A. Slavin, J. M. Raines, T. H. Zurbuchen, B. J. Anderson, H. Korth, D. N. Baker, and S. C. Solomon (2014), Ion kinetic properties in Mercury's premidnight plasma sheet, *Geophys. Res. Lett.*, *41*, 5740–5747, doi:10.1002/2014GL060468.

Gershman, D. J., J. M. Raines, J. A. Slavin, T. H. Zurbuchen, T. Sundberg, S. A. Boardsen, B. J. Anderson, H. Korth, and S. C. Solomon (2015), MESSENGER observations of multiscale Kelvin-Helmholtz vortices at Mercury, *J. Geophys. Res. Space Physics*, *120*, doi:10.1002/2014JA020903.

Gurnett, D. A., and A. Bhattacharjee (2005), *Introduction to Plasma Physic With Space and Laboratory Applications*, Cambridge Univ. Press, Cambridge, U. K.

Hu, Y., and R. E. Denton (2009), Two-dimensional hybrid code simulation of electromagnetic ion cyclotron waves in a dipole magnetic field, *J. Geophys. Res.*, *114*, A12217, doi:10.1029/2009JA014570.

Hu, Y., R. E. Denton, and J. R. Johnson (2010), Two-dimensional hybrid code simulation of electromagnetic ion cyclotron waves of multi-ion plasmas in a dipole magnetic field, *J. Geophys. Res.*, *115*, A09218, doi:10.1029/2009JA015158.

Janhunen, P., A. Olsson, A. Vaivads, and W. K. Peterson (2003), Generation of Bernstein waves by ion shell distributions in the auroral region, *Ann. Geophys.*, *21*, 881–891, doi:10.5194/angeo-21-881-2003.

Joyce, C. J., C. W. Smith, P. A. Isenberg, S. P. Gary, N. Murphy, P. C. Gray, and L. F. Burlaga (2012), Observation of bernstein waves excited by newborn interstellar pickup ions in the solar wind, *Astrophys. J.*, *745*(112), 8, doi:10.1088/0004-637X/745/2/112.

Kim, E.-H., and D.-H. Lee (2003), Resonant absorption of ULF waves near the ion cyclotron frequency: A simulation study, *Geophys. Res. Lett.*, *30*(18), 2240, doi:10.1029/2003GL017918.

Kim, E.-H., J. R. Johnson, and D.-H. Lee (2008), Resonant absorption of ULF waves at Mercury's magnetosphere, *J. Geophys. Res.*, *113*, A11207, doi:10.1029/2008JA013310.

Kim, E.-H., J. R. Johnson, and K.-D. Lee (2011), ULF wave absorption at Mercury, *Geophys. Res. Lett.*, *38*, L16111, doi:10.1029/2011GL048621.

Kim, E.-H., J. R. Johnson, K.-D. Lee, and Y. S. Pyo (2013), Field-line resonance structures in Mercury's multi-ion magnetosphere, *Earth Planets Space*, *65*, 447–451, doi:10.5047/eps.2012.08.004.

Kim, E.-H., J. R. Johnson, E. Valeo, and C. K. Phillips (2015), Global modeling of ULF waves at Mercury, PPPL Tech. Rep., PPPL-5107. [Available at http://www.pppl.gov/research/pppl-technical-reports.]

Klimushkin, D. Y., P. N. Mager, and K.-H. Glassmeier (2006), Axisymmetric Alfvén resonances in a multi-component plasma at finite ion gyrofrequency, *Ann. Geophys.*, *24*, 1077–1084, doi:10.5194/angeo-24-1077-2006.

Korth, H., B. J. Anderson, J. M. Raines, J. A. Slavin, T. H. Zurbuchen, C. L. Johnson, M. E. Purucker, R. M. Winslow, S. C. Solomon, and R. L. McNutt Jr. (2011), Plasma pressure in Mercury's equatorial magnetosphere derived from MESSENGER Magnetometer observations, *Geophys. Res. Lett.*, *38*, L22201, doi:10.1029/2011GL049451.

Korth, H., B. J. Anderson, D. J. Gershman, J. M. Raines, J. A. Slavin, T. H. Zurbuchen, S. C. Solomon, and R. L. McNutt Jr. (2014), Plasma distribution in Mercury's magnetosphere derived from MESSENGER Magnetometer and Fast Imaging Plasma Spectrometer observations, *J. Geophys. Res. Space Physics*, *119*, 2917–2932, doi:10.1002/2013JA019567.

Menietti, J. D., O. Santolik, J. D. Scudder, J. S. Pickett, and D. A. Gurnett (2002), Electrostatic electron cyclotron waves generated by low-energy electron beams, *J. Geophys. Res.*, *107*(A10), 1285, doi:10.1029/2001JA009223.

Ogilvie, K. W., J. D. Scudder, V. M. Vasyliunas, R. E. Hartle, and G. L. Siscoe (1977), Observations at the planet Mercury by the plasma electron instrument: Mariner 10, *J. Geophys. Res.*, *82*, 1807–1824, doi:10.1029/JA082i013p01807.

Omidi, N., R. Thorne, and J. Bortnik (2011), Hybrid simulations of EMIC waves in a dipolar magnetic field, *J. Geophys. Res.*, *116*, A09231, doi:10.1029/2011JA016511.

Omidi, N., J. Bortnik, R. Thorne, and L. Chen (2013), Impact of cold O+ ions on the generation and evolution of EMIC waves, *J. Geophys. Res. Space Physics*, *118*, 434–445, doi:10.1029/2012JA018319.

Othmer, C., K. H. Glassmeier, and R. Cramm (1999), Concerning field line resonances in Mercury's magnetosphere, *J. Geophys. Res.*, *104*, 10,369–10,378, doi:10.1029/1999JA900009.

Perraut, S., A. Roux, P. Robert, R. Gendrin, J.-A. Sauvaud, J.-M. Bosqued, G. Kremser, and A. Korth (1982), A systematic study of ULF waves above FH+ from GEOS 1 and 2 measurements and their relationships with proton ring distributions, *J. Geophys. Res.*, *87*(A8), 6219–6236, doi:10.1029/JA087iA08p06219.

Raines, J. M., J. A. Slavin, T. H. Zurbuchen, G. Gloeckler, B. J. Anderson, D. N. Baker, S. M. Krimigis, H. Korth, and R. L. McNutt Jr. (2011), MESSENGER observations of the plasma environment near Mercury, *Planet. Space Sci.*, *59*, 2004–2015, doi:10.1016/j.pss.2011.02.004.

Raines, J. M., et al. (2013), Distribution and compositional variations of plasma ions in Mercury's space environment: The first three Mercury years of MESSENGER observations, *J. Geophys. Res. Space Physics*, *118*, 1604–1619, doi:10.1029/2012JA018073.

Rönnmark, K. (1982), WHAMPS: Waves in homogeneous, anisotropic multicomponent plasmas, Report 179, Kiruna Geophys. Inst., Kiruna, Sweden.

Rönnmark, K. (1983a), Computation of the dielectric tensor of a Maxwellian plasma, *Plasma Phys.*, *25*, 699, doi:10.1088/0032-1028/25/6/007.

Rönnmark, K. (1983b), Emission of myriametric radiation by coalescence of upper hybrid waves with low-frequency waves, *Ann. Geophys.*, *1*, 187.

Rönnmark, K. (1984), Ray tracing in dissipative media, *Ann. Geophys.* (ISSN 0755–0685), *2*, 57–60.

Rönnmark, K., and M. André (1991), Convection of ion cyclotron waves to ion-heating regions, *J. Geophys. Res.*, *96*(A10), 17,573–17,579, doi:10.1029/91JA01793.

Russell, C. T. (1989), ULF waves in the Mercury magnetosphere, *Geophys. Res. Lett.*, *16*, 1253–1256, doi:10.1029/GL016i011p01253.

Schmidt, G. (1979), *Physics o f High Temperature Plasmas*, Academic, San Diego, Calif.

Slavin, J. A., et al. (2008), Mercury's magnetosphere after MESSENGER's first flyby, *Science*, *321*, 85–89, doi:10.1126/science.1159040.

Slavin, J. A., et al. (2009), MESSENGER observations of magnetic reconnection in Mercury's magnetosphere, *Science*, *324*, 606–610, doi:10.1126/science.1172011.

Suchy, K. (1981), Real Hamilton equations of geometric optics for media with moderate absorption, *Radio Sci.*, *16*, 1179, doi:10.1029/RS016i006p01179.

Wang, C.-P., M. Gkioulidou, L. R. Lyons, and V. Angelopoulos (2012), Spatial distributions of the ion to electron temperature ratio in the magnetosheath and plasma sheet, *J. Geophys. Res.*, *117*, A08215, doi:10.1029/2012JA017658.

Whitman, G. B. (1999), *Linear and Nonlinear Waves*, Wiley, New York.

Winske, D., and N. Omidi (1993), Hybrid codes: Methods and applications, in *Computer Space Plasma Physics: Simulation Techniques and Software*, edited by H. Matsumoto and Y. Omura, 103 pp., Terra Sci, Tokyo.

Wu, S., R. E. Denton, and W. Li (2013), Effects of cold electron density on the whistler anisotropy instability, *J. Geophys. Res. Space Physics*, *118*, 765–773, doi:10.1029/2012JA018402.